Monthly Notices
of the
ROYAL ASTRONOMICAL SOCIETY

Mon. Not. R. Astron. Soc. **402,** 1959–1968 (2010) doi:10.1111/j.1365-2966.2009.16022.x

Mapping the $\nu_\odot$ secular resonance for retrograde irregular satellites

J. Correa Otto,⋆ A. M. Leiva, C. A. Giuppone and C. Beaugé

Observatorio Astronómico, Universidad Nacional de Córdoba, Laprida 854, (X5000BGR) Córdoba, Argentina

Accepted 2009 November 10. Received 2009 November 5; in original form 2009 October 15

ABSTRACT

Constructing dynamical maps from the filtered output of numerical integrations, we analyse the structure of the $\nu_\odot$ secular resonance for fictitious irregular satellites in retrograde orbits. This commensurability is associated with the secular angle $\theta = \varpi - \varpi_\odot$, where ϖ is the longitude of the pericentre of the satellite and $\varpi_\odot$ corresponds to the (fixed) planetocentric orbit of the Sun. Our study is performed in the restricted three-body problem, where the satellites are considered as massless particles around a massive planet and perturbed by the Sun.

Depending on the initial conditions, the resonance presents a diversity of possible resonant modes, including librations of θ around 0 (as found for Sinope and Pasiphae) or 180° as well as asymmetric librations (e.g. Narvi). Symmetric modes are present in all giant planets, although each regime appears restricted to certain values of the satellite inclination. Asymmetric solutions, on the other hand, seem absent around Neptune due to its almost circular heliocentric orbit.

Simulating the effects of a smooth orbital migration on the satellite, we find that the resonance lock is preserved as long as the induced change in the semimajor axis is much slower compared to the period of the resonant angle (adiabatic limit). However, the librational mode may vary during the process, switching between symmetric and asymmetric oscillations.

Finally, we present a simple scaling transformation that allows us to estimate the resonant structure around any giant planet from the results calculated around a single primary mass.

Key words: celestial mechanics – planets and satellites: general.

1 INTRODUCTION

Both Jupiter and Saturn are rich in irregular satellites. Jupiter has at least 54 moons in this group, while Saturn contains more than 30 members. A smaller population is also observed around Uranus and Neptune, although it is not clear whether this is intrinsic or due to observational bias (Nicholson et al. 2008).

Irregular satellites suffer strong perturbations from the Sun which significantly affect the evolution of their orbits. Whipple & Shelus (1993) numerically integrated the orbit of the Jovian moon Pasiphae for 10^5 years under the effects of all planets and found that its longitude of pericentre ϖ is locked in a secular resonance where $\varpi - \varpi_{\rm Jup}$ librates around 180°. Here $\varpi_{\rm Jup}$ is the longitude of pericentre of the heliocentric orbit of Jupiter. Since $\varpi_{\rm Jup} = \varpi_\odot + \pi$, where $\varpi_\odot$ is the Jupiter-centric longitude of the pericentre of the Sun, this implies that $\varpi - \varpi_\odot$ oscillates around zero. By analogy from asteroidal motion, we will call this the ν_5 secular resonance for satellite orbits.

In the same year, Saha & Tremaine (1993) found that the Jovian moon Sinope also displays a similar resonance lock in the ν_5 resonance, although in this case the motion alternates between libration and circulation on time-scales of the order of 10^5–10^6 years. Extending the orbital evolution for 5×10^7 years, Nesvorný et al. (2003) showed that Pasiphae's libration is also temporary and will switch to a circulation of the resonant angle in approximately 3×10^7 years.

Ćuk & Burns (2004) performed a detailed search for other irregular moons in secular resonances, finding that the prograde Saturn moon Siarnaq appears to the trapped in a pericentre secular resonance with Saturn (i.e. ν_6), also displaying intermittent libration, where the resonant angle oscillates around 180°. While the Uranus irregular satellite Stephano is not in libration, the angle $\varpi - \varpi_\odot$ shows a quasi-resonant behaviour with a very long-period circulation.

Finally, Beaugé & Nesvorný (2007) found that although the retrograde Saturn moon Narvi is not currently in resonant motion, long-term simulations show a future libration in the ν_6 secular resonance. Contrary to previous cases, here the resonant angle displays libration around values different from 0 or 180°, in what appears to be an asymmetric libration point. Since all these resonant

⋆E-mail: jorgecorrea@oac.uncor.edu

configurations, independently of the planetary mass, involve the relative behaviour of the longitude of the pericentre of the satellite and that of the planetocentric orbit of the Sun, in all future references we will denote this commensurability as $\nu_\odot$.

At present, it is not clear whether the observed resonant population in the outer planets is evidence of a past smooth orbital migration of the satellites or whether it is simply due to chance. Beaugé & Nesvorný (2007) found that stability criteria alone yield satellite populations close to $\nu_\odot$, although the proximity of some individual moons (particularly Pasiphae and Sinope) appears sufficiently detached from a random distribution to be statistically significant.

One of the problems in understanding a possible relationship between the $\nu_\odot$ resonance and the past evolution of the irregular satellites is the lack of a detailed analysis of the resonant structure. As will be shown in Section 2, analytical models, even of high order, are not sufficiently precise and are unable to reproduce the main characteristics of the secular commensurability. Semi-analytical models, where the secular perturbations are evaluated by numerical averaging of the exact Hamiltonian, also suffer the same limitations since they are equivalent to a first-order theory. For this reason, so far most of the dynamical studies have been restricted to numerical integrations of individual orbits.

In this paper, we present a numerical study of the structure of the $\nu_\odot$ resonance for retrograde orbits. The resonant behaviour is obtained applying two filters to the numerical output; the first one is constructed to eliminate the short-period variations (frequencies comparable with the mean motions). The resulting data are then filtered once again to reduce the effects caused by the non-resonant secular angular variable. The results are displayed as dynamical maps showing the location, type and extension of the librational domains for several values of the integrals of motion.

The details of the numerical method are outlined in Section 3, which includes an application to the region of the phase space in the vicinity of the Jovian moon Sinope. Section 4 shows the structure of the $\nu_\odot$ resonance in the Saturn system. In both cases, the maps are constructed for a single value of the proper semimajor axis. Section 5 discussed the effects of an ad hoc migration acting of the satellites orbits and its effects on the resonant motion. Next, in Section 6 we present a simple scaling law that allows us to relate the resonant structure for any planetary mass. Finally, the application of the real satellites is briefly discussed in Section 7 while concluding remarks are given in Section 8.

2 ANALYTICAL MODELS FOR THE $\nu_\odot$ RESONANCE

Assume a fictitious satellite in an orbit around a giant planet m_p perturbed by the Sun. Let a be the satellite's planetocentric semimajor axis, e its eccentricity, i its inclination with respect to the Laplace plane, M the mean anomaly, ω the argument of the pericentre and Ω the longitude of the node. Planetocentric orbital elements of the Sun will be identified by the index $\odot$. Since we will adopt a Hamiltonian approach, it is useful to introduce the modified Delaunay canonical variables:

$$\begin{aligned} L &= \sqrt{\mu a} \quad ; M \\ G &= L\sqrt{1-e^2} \; ; \omega \\ H &= G\cos i \quad ; \Omega. \end{aligned} \tag{1}$$

The complete Hamiltonian function can then be written as $F = F_0(L, \Lambda) + R$, where F_0 is the two-body contribution (Λ is the canonical momenta associated with $\mathrm{M}_\odot$) and $R = R(L, G, H, M, \omega, \Omega, M_1)$ denotes the disturbing function stemming from the solar gravitational effects. R also depends on the orbital elements of the Sun ($e_\odot, i_\odot, \varpi_\odot$ and $\Omega_\odot$), which are considered constant, as well as on the planetary (i.e. central) mass m_p.

Yokoyama et al. (2003) presented an analytical model for the secular behaviour of irregular satellites in the restricted three-body problem and applied it to the Jovian satellite system. It is based on Kaula's (1962) expansion of the disturbing function, truncated at fourth order in $\alpha = a/a_\odot$ and eccentricities and inclinations. The averaging over the short-period terms, associated with the mean anomalies of both bodies, is done to first order. We will denote as F_1 the resulting expression of the secular Hamiltonian.

Although we will not write the expression explicitly, functionally it can be written as $F_1 = F_1(G^*, H^*, \omega^*, \Omega^*; \alpha^*)$, where the new (starred) variables are the mean elements, which must not be mistaken with the original osculating variables. The quantity α^* is related to the 'proper' Delaunay momenta L^* by the equation $\alpha^* = L^{*2}/\mu a_\odot$.

To study a given secular resonance, we must perform a canonical transformation to resonant variables. The $\nu_\odot$ commensurability is defined by the angle $\theta = \varpi - \varpi_\odot$; however, the relationship between the argument of pericentre ω and the longitude of pericentre ϖ is different when considering direct or retrograde orbits. Since most of the real irregular satellites in the vicinity of this resonance are retrograde, we will assume $i > 90^\circ$, for which $\varpi = \Omega - \omega$.

Our set of resonant variables will be (I_1, I_2, ϕ, Q), where $\phi = \Omega^* - \omega^*$ will be a slow angle related to θ, while Q is a fast angle. This can be chosen among any linear combination of the secular angles with the only condition being that it be independent of ϕ. For this work, we will choose $Q = \Omega^*$ and check that the precessional frequency of the longitude of the node is higher than the frequency of ϕ. Having specified the angles, the expressions for the corresponding canonical momenta can be easily found. The complete transformation from the mean Delaunay variables to the resonant counterparts is given by

$$\begin{aligned} I_1 &= -G^*, \qquad \phi = \Omega^* - \omega^* \\ I_2 &= G^* + H^*, \quad Q = \Omega^*. \end{aligned} \tag{2}$$

The resonant angle would then be $\theta = \phi - \varpi_\odot$.

The transformation of the secular Hamiltonian to resonant variables is straightforward, yielding $F_1(I_1, I_2, \theta, Q)$. Since Q is a fast variable, we can perform a first-order averaging of the Hamiltonian over this angle. This averaging implies a new canonical transformation to new resonant variables $(I_1^*, I_2^*, \theta^*, Q^*)$ such that the transformed Hamiltonian $F_1^* = F_1^*(I_1^*, \theta^*; I_2^*)$ and Q^* is cyclic. The associated momenta I_2^* are then a new constant of motion, and the system is reduced to a single-degree of freedom model for the $\nu_\odot$ resonance in the canonical pair (I_1^*, θ^*).

Equation (10) of Yokoyama et al. (2003) gives explicit expressions for F_1^*, which can be succinctly written as

$$F_1^* = A_0 + A_1\cos(\theta^*) + A_2\cos(2\theta^*), \tag{3}$$

where the coefficients $A_k = A_k(I_1^*; L^*, I_2^*)$ are a function of the resonant momenta I_1^* and parametrized by the constants L^*, I_2^* and the orbital elements of the Sun. Different initial conditions will give different values of the proper elements L^*, I_2^*.

2.1 The secular dynamics of Sinope

As an example, Fig. 1(a) shows the level curves of constant F_1^* in the plane (θ^*, e^*), adopting Jupiter as the central body (i.e. m_p). The quantity $e^* = e^*(I_1^*; L^*, I_2^*)$ is the so-called mean–mean eccentricity,

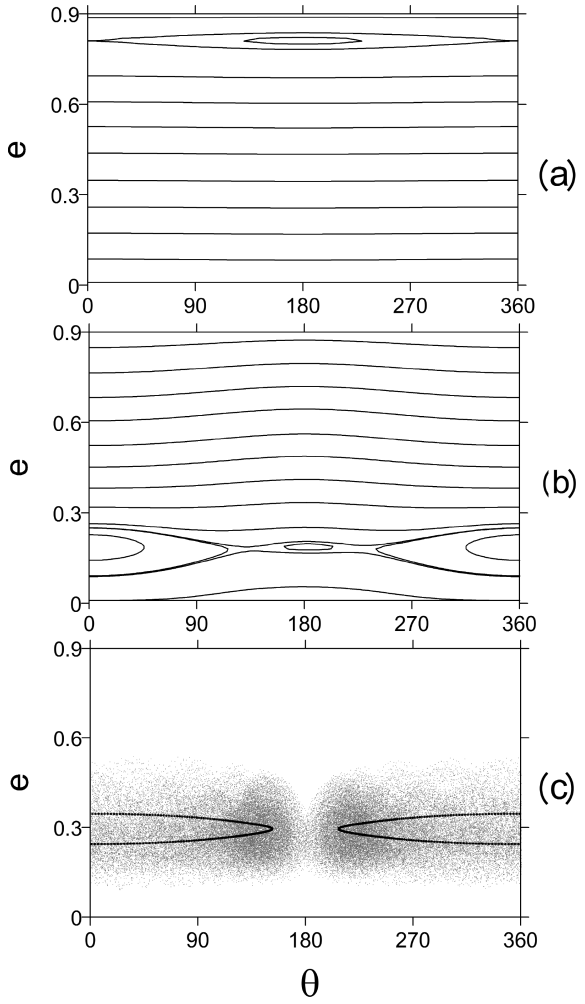

Figure 1. (a) Level curves of constant Hamiltonian F_1^* for the Jovian $\nu_\odot$ resonance, in the plane (e^*, θ^*), using a first-order averaging over short-period terms. The adopted values for the integrals of motion are $L^* = 2.115 \times 10^{-4}$, $I_2^* = 1.575 \times 10^{-5}$, in units of $M_\odot$, au and day, respectively. These values correspond to the Jovian satellite Sinope. (b) Same as before, but for the third-order Hamiltonian F_3^*. (c). Numerical simulation of *Sinope* (three-body problem) over 10^5 years. Grey dots show the evolution of the osculating elements while black dots correspond to an output filtered to eliminate all periodic variations with a period smaller than 100 years.

which can be obtained from the canonical momenta I_1^* assuming that the values of L^*, I_2^* are constant for all initial conditions. The adopted values for these parameters are close to the irregular satellite Sinope and were calculated from a numerical simulation of the exact equations (three-body problem) over a time-span of 10^5 years.

For these constants, the phase plane of F_1^* shows a resonance region centred approximately at $e^* \simeq 0.85$ corresponding to a libration of θ^* around 180°. The width of the libration zone is approximately $\Delta e \sim 0.05$. All initial conditions with lower values of the eccentricity correspond to circulations. This structure contrasts significantly with Fig. 1(c) which shows the real dynamical behaviour of Sinope obtained with the same numerical simulation described previously. The values of (θ^*, e^*) were calculated using a low-pass far-infrared (FIR) digital filter (Carpino, Milani & Nobili 1987) to eliminate all periodic variations with a period smaller than 100 years. This includes variations in the orbital elements due to both the mean anomalies and Ω. For comparison, we also show the evolution of the osculating elements in grey dots. A comparison between both the figures shows that the analytical model F_1^* fails to reproduce the correct dynamics of the system, predicting that Sinope should be far from the resonance domain displaying a circulation of θ^*.

This imprecision is not restricted to the structure of the phase space in the vicinity of this satellite, but is a general flaw of the averaging process used to obtain the analytical model. As shown by Ćuk & Burns (2004), averaging over short-period terms must be performed to order higher than unity, to include the effect of second- and third-order secular terms such as evection. These effects cause significant variations in the secular frequencies, thus affecting the long-term evolution of individual bodies, calculations of including proper elements and the location of the secular resonances in the domain of irregular satellites.

With this in mind, Beaugé, Michtchenko & Ferraz-Mello (2006a) developed a high order analytical model of the secular Hamiltonian for irregular satellites, where the averaging process over the mean anomalies was extended to third order. The new Hamiltonian function, which we will refer to as $F_3 = F_3(G^*, H^*, \omega^*, \Omega^*; \alpha^*)$, was used to calculate the proper elements of all irregular satellites of the outer planets and estimate their proximity to different secular resonances (Beaugé & Nesvorný 2007).

From the analytical expression of F_3, we can now construct a higher order model for the $\nu_\odot$ resonance in the same manner as before and plot the level curves of F_3^* in the vicinity of Sinope. Results are shown in Fig. 1(b) and show a significant improvement with respect to F_1. The resonance domain is now much closer to the actual orbit of the Jovian satellite, and the main libration island is now (correctly) associated with an oscillation around $\theta^* = 0$. However, some important discrepancies still remain. The centre of the libration region is still not correct, and the analytical model now predicts a smaller eccentricity than the numerical simulation. More important, F_3^* shows a secondary libration island around $\theta^* = 180°$ which in fact does not exist. As shown in fig. 16 of Beaugé & Nesvorný (2007) the size of this second libration mode increases for larger values of I_2^*, becoming an important characteristic of the phase space for librations at high eccentricities.

2.2 Estimation of the secular frequencies

The top and middles plots of Fig. 2 show the frequencies of the secular angles ω^*, Ω^* (denoted by ν_ω and ν_ω, respectively) as a function of the proper eccentricity e^*, with initial conditions corresponding to the same values of the integrals L^* and I_2^* as before. Dashed curves show the results obtained using the analytical Hamiltonian F_1^* restricted to those terms which depend only on the canonical momenta. Frequencies calculated with the third-order function F_3^* are shown in continuous lines. For comparison, we also estimated the same frequencies numerically (open circles) by Fourier analysing the filtered output of a series of simulations for 10^5 years.

For both ω^* and Ω^* there is a very marked offset between the real frequencies and the results obtained through F_1^*, and the analytical estimates systematically yield lower values. A better agreement is noted using F_3^*, especially for the precessional frequency of the node, although a larger discrepancy is noted for the argument of the pericentre. It is also important to recall that both analytical models were developed using Kaula's expansion of the disturbing function, whose convergence is only guaranteed for eccentricities below ∼0.6 (e.g. Wintner 1941). This seems to be the cause of the increasing imprecision of F_3^* for values of e^* approaching this limit, but also implies that the results obtained with the simpler model F_1^* are undependable for $e^* > 0.6$.

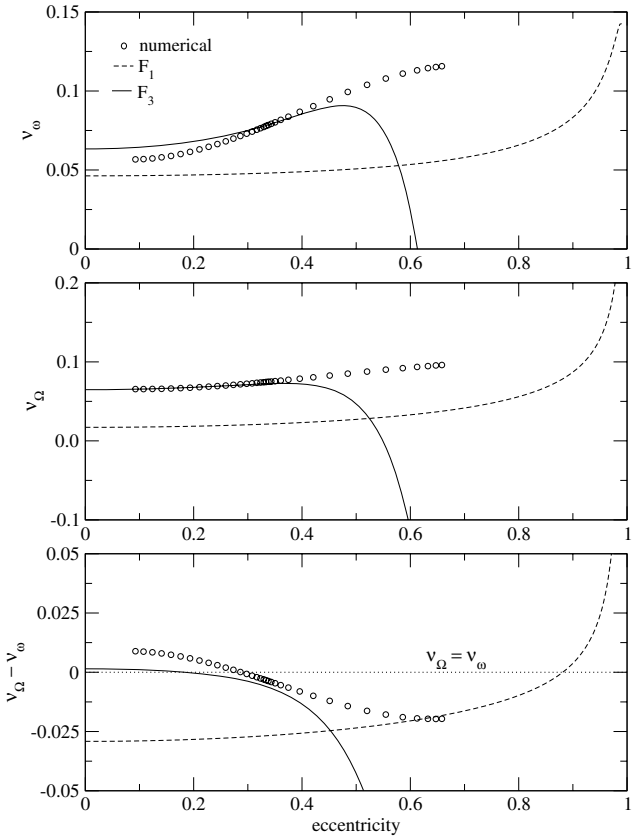

Figure 2. Frequencies of the secular angles ω^*, Ω^* and $\phi = \Omega^* - \omega^*$, obtained with both analytical Hamiltonians (continuous and dashed curves). Open circles show numerical results calculated from a Fourier analysis of filtered data. All initial conditions correspond to the same values of L^* and I_2^* as in Fig. 1.

The bottom graph of Fig. 2 shows the values of $\nu_\Omega - \nu_\omega$ for the same initial conditions. Zero values (dotted line) correspond to the exact $\nu_\odot$ resonance, since we are considering constant longitude of the pericentre for Jupiter's orbit. This plot shows how the imprecision in the secular frequencies affect the resonance location. For F_1^* the exact resonance occurs for almost parabolic orbits, well beyond the convergence limit of the expansion of the disturbing function, and thus its very existence appears unreliable. Once again better agreement is noted using F_3^*, although a significant error is still in evidence. Notwithstanding, since the continuous curve is very shallow for low eccentricities, even small differences in the model can cause important displacements in the location of the exact resonance.

3 THE NUMERICAL MODEL

Outside secular resonances, analytical models constitute adequate tools for the long-term dynamics of irregular satellites and can be used to obtain fairly precise proper elements for real bodies (Beaugé & Nesvorný 2007). They are also able to reproduce the structure and location of the Lidov–Kozai resonance (Lidov 1961; Kozai 1962) with good precision. However, even high order analytical models seem insufficient for the task of mapping the structure of other secular resonances, such as the $\nu_\odot$ commensurability. Not only the location of the resonance domain may be imprecise, but the libration centres and secondary modes predicted by the models may also be unreliable.

In this section we will present a series of dynamical maps of the Jovian $\nu_\odot$ resonance, obtained numerically by filtering the outputs of a series of long-term simulations of fictitious particles. Each map consists of the dynamical evolution of a set of initial conditions with pre-defined values of the integrals $(\bar{L}^*, \bar{I}_2^*)$. The main advantage of this procedure over analytical expansions is that we are no longer restricted to low to moderate eccentricities, and there are no approximations in the modelling of the gravitational interactions. As before, we will work in the realm of the restricted three-body problem and assume a fixed orbit for the planetocentric motion of the Sun.

For each map, we begin with a set of initial conditions in osculating orbital elements for the particle plus the mean anomaly of the Sun $(a, e, i, M, \mathrm{M}_\odot, \omega, \Omega)$. Each orbit is integrated for a time span of 10^5 years using a Burlisch–Stoe-based N-body code. The output is subsequently converted to canonical resonant variables $(L, I_1, I_2, M, \mathrm{M}_\odot, \phi, Q)$ and filtered to eliminate the variations associated with the mean anomalies M and $\mathrm{M}_\odot$ as well those corresponding to the fast variable Q. Although the orbital periods of both bodies are well known beforehand, the frequency of Q may depend on the initial condition and must be monitored closely. Thus, the decimation and length of the filter may change in each simulation. However, we have found that a cut-off period of 200 years and a filter of 1600 data points gave very precise results in most cases.

The output of the filtering is a numerical approximation to the transformed resonant variables $(I_1^*, \phi^*; L^*, I_2^*)$, analogous to those obtained with an analytical model, with one important difference. Although the digital filtering can be considered analogous to an averaging of the short-period angles, it does not reduce the number of degrees of freedom of the system. Consequently, any chaoticity in the original solution will be preserved in the filtered data. This implies that a regular (non-chaotic) solution will give a one-dimensional curve in the (I_1^*, ϕ^*) plane, while a stochastic trajectory will cover a two-dimensional region.

To construct the map, each set of initial conditions in osculating variables must yield the same values of $(L^*, I_2^*) = (\bar{L}^*, \bar{I}_2^*)$. From perturbation theory, we know that

$$
\begin{aligned}
L^* &= L + \frac{\partial}{\partial M}\chi = f_1(a, e, i, M, \mathrm{M}_\odot, \omega, \Omega) \\
I_2^* &= I_2 + \frac{\partial}{\partial Q}\chi = f_2(a, e, i, M, \mathrm{M}_\odot, \omega, \Omega),
\end{aligned}
\tag{4}
$$

where $\chi(L, I_1, I_2, M, \mathrm{M}_\odot, \phi, Q)$ is the generating function written in osculating variables evaluated at the initial conditions. Analytical models allow explicit construction of function χ, which can be inverted to give the necessary values of the osculating elements. Since numerical simulations do not give f_i, the inversion of expressions (4) must be done by iterations.

The idea is to introduce small deviations in the osculating variables $a \rightarrow \mathrm{a} + \Delta a$ and $i \rightarrow \mathrm{i} + \Delta i$ and leave all the other initial conditions intact. Introducing these expressions in (4) and expanding f_i in a first-order Taylor expansion around the original values, we obtain

$$
\begin{aligned}
L^* + \Delta L^* &= L^* + \frac{\partial f_1}{\partial a}\Delta a + \frac{\partial f_1}{\partial i}\Delta i \\
I_2^* + \Delta I_2^* &= I_2^* + \frac{\partial f_2}{\partial a}\Delta a + \frac{\partial f_2}{\partial i}\Delta i,
\end{aligned}
\tag{5}
$$

where the partial derivatives of f_i are evaluated at the initial orbital set. Equating $L^* + \Delta L^* = \bar{L}^*$ and $I_2^* + \Delta I_2^* = \bar{I}_2^*$, equations (5) can be inverted to give the necessary values of Δa and Δi. The partial derivatives can be estimated numerically using finite differences, calculating how the integrals vary with very small deviations in each

of the orbital elements around the original values. This procedure is not very precise, but successive approximations can be used to give the desired solution. In general, a few iterations are sufficient to give values with relative precision of the order of $\Delta L^*/\bar{L}^*$, $\Delta I_2^*/\bar{I}_2^* \sim 10^{-4}$.

3.1 Resonance maps around Sinope

Fig. 3 shows several dynamical maps constructed for $L^* = 2.115 \times 10^{-4}$ (corresponding to $a^* = 0.16$ au) and four different values of I_2^*. For simplification purposes, all numerical values of I_2^* will be given in units of 10^{-5}. The lower left-hand frame roughly corresponds to the initial conditions of Sinope. Instead of plotting I_1^* as a function of the resonant angle θ^*, we converted the canonical momenta to equivalent mean–mean eccentricities e^* and inclinations i^* according to the relationships

$$I_1^* = -G^* = -L^*\sqrt{1-e^{*2}}$$
$$I_2^* = G^* + H^* = I_1^*(1+\cos i^*). \quad (6)$$

In all the plots, we note a main libration island centred around $\theta^* = 0$, although the map for $I_2^* = 1.0$ also shows a small libration region centred at $\theta^* = 180^\circ$. The values of i^* and e^* of the centre of each main libration island are shown in Fig. 4, where the error bars indicate the libration width in each orbital element. The libration zone appears extensive in the eccentricity, although it decreases in size for larger values of I_2^*. However, the corresponding size in i^* is very small, indicating that the $\nu_\odot$ commensurability appears very restricted in the inclination.

Although most orbits in Fig. 3 appear regular, the map for $I_2^* = 3.0$ shows some irregular trajectories which appear to indicate chaotic motion. To test this, we integrated 200 initial conditions for every value of I_2^*. Each had a different initial value of I_1^*, and the initial value of the resonant angle θ^* was taken to be equal to zero. The total integration time was 10^6 years and, together with the equations of motion, we also calculated the MEGNO (Mean Exponential Growth Factor of Nearby Orbits; Cincotta & Simó 2000) chaoticity indicator. Fig. 5 shows the values of the averaged MEGNO number $\langle Y \rangle$ as a function of the mean–mean eccentricity for each map. Regular orbits yield $\langle Y \rangle \leq 2$ while larger values are indicative of chaotic motion (see Cincotta & Simó 2000 for more details). Unstable orbits, leading to an ejection of the particle in the integrated time-span, was assigned a value of $\langle Y \rangle = 10$. The extent of the libration island is shown as a shaded rectangle.

For low values of I_2^*, the chaotic region is restricted to high eccentricities and far from the secular resonance region. Thus, all commensurate trajectories are indeed regular, at least in the time

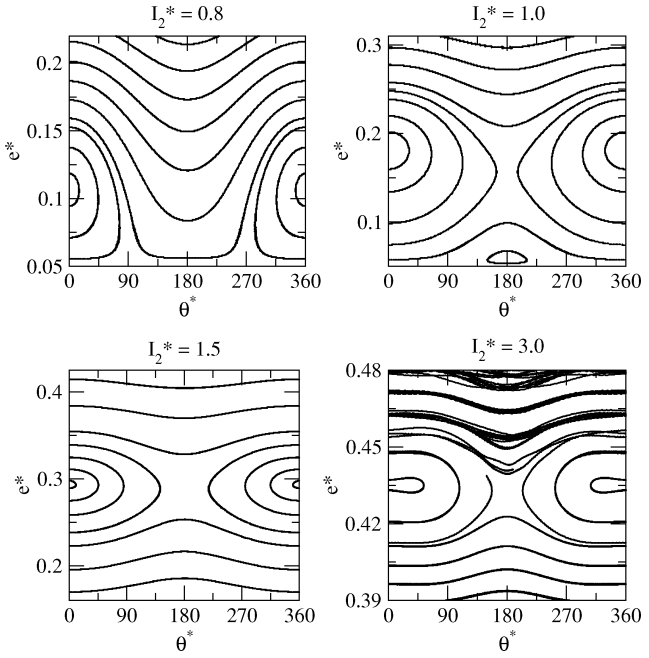

Figure 3. Filtered output, in the (e^*, θ^*) plane, of a series of numerical integrations with initial conditions leading to $a^* = 0.16$ au ($L^* = 2.115 \times 10^{-4}$) and four different values of I_2^* (in units of 10^{-5}). Each plot is roughly centred on the libration domain of the Jovian $\nu_\odot$ resonance. Chaotic motion is noticeable in the lower right-hand plot, especially for values of e^* larger than the centre of libration.

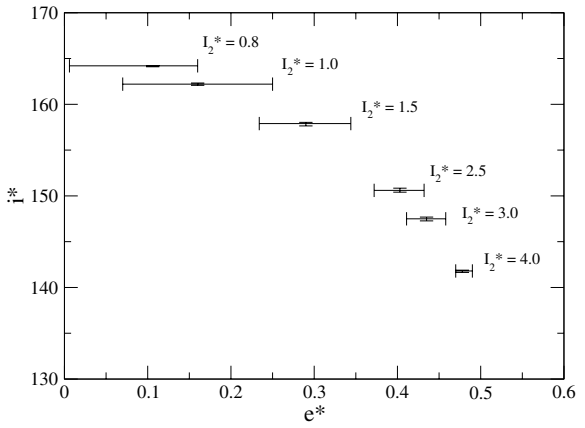

Figure 4. Values of i^* and e^* corresponding to the centre of the libration island for different values of I_2^*. Error bars indicate the libration width in each orbital element.

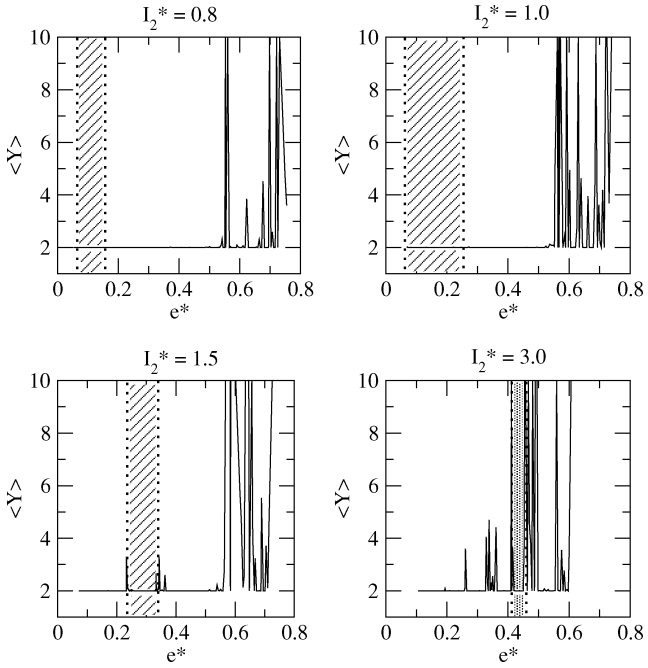

Figure 5. Averaged MEGNO indicator $\langle Y \rangle$ for 200 initial conditions with $\theta^* = 0$ in the four dynamical maps shown previously. Regular orbits are characterized by $\langle Y \rangle \leq 2$ while larger values are indicative of chaotic motion. Unstable orbits were given a value of $\langle Y \rangle = 10$. In each plot, the libration region is shaded.

interval analysed. For $I_2^* = 1.5$, the stochasticity of the resonance separatrix is clearly visible. However, for $I_2^* = 3.0$ the chaos is much more extensive and covers the Jovian $\nu_\odot$ resonance zone. This helps to explain why the dynamical map constructed for this value of I_2^* showed irregular trajectories in the (e^*, θ^*) plane. A simple analysis of the output in osculating elements shows that the stochasticity is caused by the 6/1 mean-motion resonance with the planetocentric orbit of the Sun. As shown recently by Hinse, Christou & Alvarellos (2009), the retrograde satellite region in the Jovian system is affected by several mean-motion commensurabilities. Even though they appear to be of high order, the interaction with the secular resonance gives origin to a noticeable chaotic behaviour.

4 RESONANCE MAPS IN THE SATURN SATELLITE SYSTEM

Since the Jovian satellite system is tainted with chaos stemming from mean-motion resonances, we switched planets and analysed the structure of the $\nu_\odot$ commensurability in Saturn. Beaugé & Nesvorný (2007) found that although the irregular satellite Narvi is not currently in a resonant configuration, the effects of the other outer planets will cause temporary trapping in the $\nu_\odot$ resonance in the future. Contrary to both Sinope and Pasiphae in the Jupiter system, the resonant behaviour of Narvi appears to correspond to an asymmetric libration of θ^*.

Taking the orbital elements of Narvi as a starting point, we constructed resonance maps for Saturn in an analogous manner to those constructed for Jupiter. In this case the proper semimajor axis was $a^* = 0.13$ au (corresponding to $L^* = 1.04 \times 10^{-4}$), and we varied I_2^* from 1.0 to 3.0 (in units of 10^{-5}). For each value of I_2^*, we searched for initial conditions with different values of I_1^*. The results were filtered to eliminate the short-period terms associated with the mean anomalies and the variations due to the precession of the longitude of the node. Results are shown in Figs 6 and 7. The

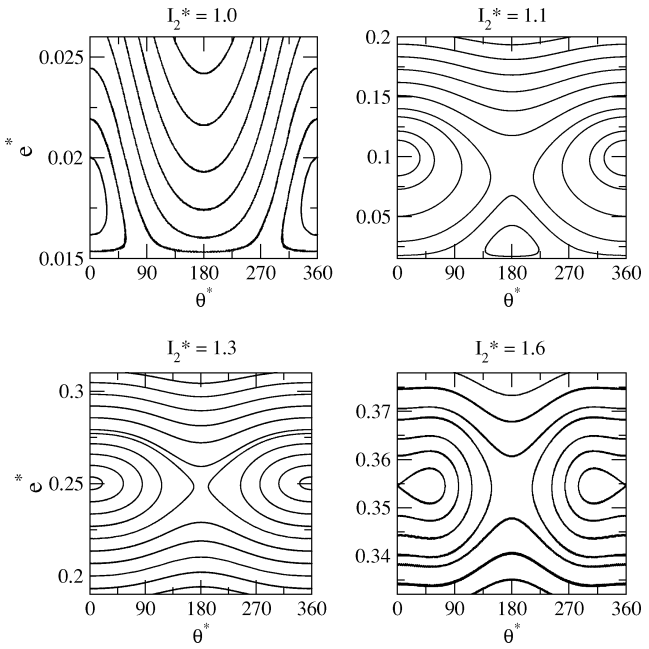

Figure 6. Structure of the $\nu_\odot$ resonance for initial conditions around the Saturn irregular satellite Narvi. Each plot shows filtered output, in the (e^*, θ^*) plane, of a series of numerical integrations with initial conditions leading to $a^* = 0.13$ au and four different values of I_2^* (in units of 10^{-5}).

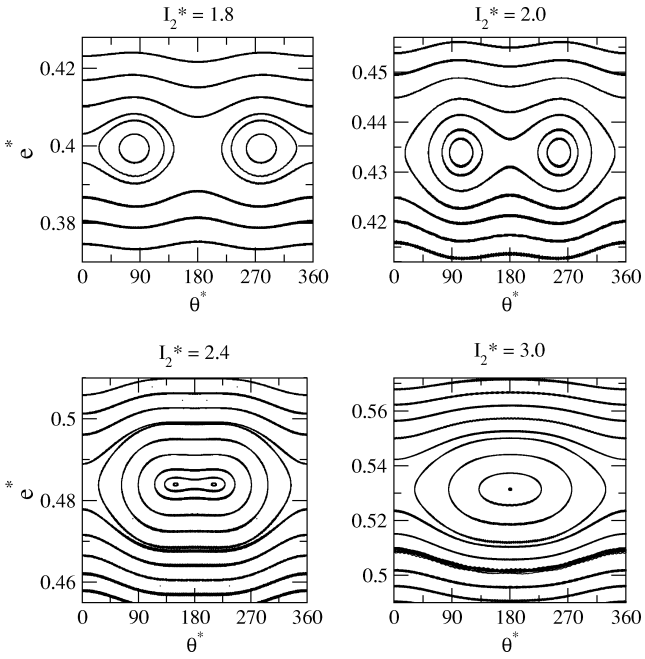

Figure 7. Same as the previous plot, for larger values of I_2^*.

first figure corresponds to lower values of I_2^* and shows significant similarities with the maps constructed for Jupiter (Fig. 3). Libration at low eccentricities is associated with a libration around $\theta^* = 0$, although for $I_2^* = 1.6$ we note that the symmetric solution turns unstable and bifurcates into two islands of asymmetric libration.

The asymmetric structure appears more evident in the top left-hand plot of Fig. 7 ($I_2^* = 1.8$). There are now two separatrices: an exterior homoclinic curve which stems from $\theta^* = 180^\circ$ and surrounds the whole resonant domain and an interior separatrix centred around $\theta^* = 0$ that encompasses the asymmetric libration centres. The order is inverted in the next plot, constructed for $I_2^* = 2.0$, and now the critical curve associated with $\theta^* = 0$ appears exterior in the resonance domain. As I_2^* increases, the equilibrium values of θ^* move towards $\theta^* = 180^\circ$ until a new bifurcation is noted to $I_2^* \sim 2.8$. From this point onwards the libration returns to a symmetric solution, this time around $\theta^* = 180^\circ$.

It is interesting to note the change in the topology of the resonance as a function of I_2^* and, consequently, as a function of the value of e^* associated with the centre of the libration domain. Previous studies of the $\nu_\odot$ commensurability only showed a libration around $\theta^* = 0$ and, in the case of Narvi, a possible asymmetric libration. The complete structure is far more complex. Fig. 8 shows the values of i^* and e^* corresponding to the centre of the main libration island for different values of I_2^*. The same general trend is observed as in Fig. 4, where once again the resonance region appears restricted to mean–mean eccentricities below $e^* \sim 0.55$ for high values of the orbital inclinations.

Finally, no significant chaos was found for these initial conditions, indicating that the $\nu_\odot$ resonance appears more stable for Saturn than for Jupiter. At least in part, this is due to the larger value of $a_\odot$ which pushes the dynamically significant mean-motion resonances much further from the planet.

5 SATELLITE MIGRATION

So far we have only analysed the resonant structure in Saturn for a given value of L^*, corresponding to $a^* = 0.13$ au. Since the

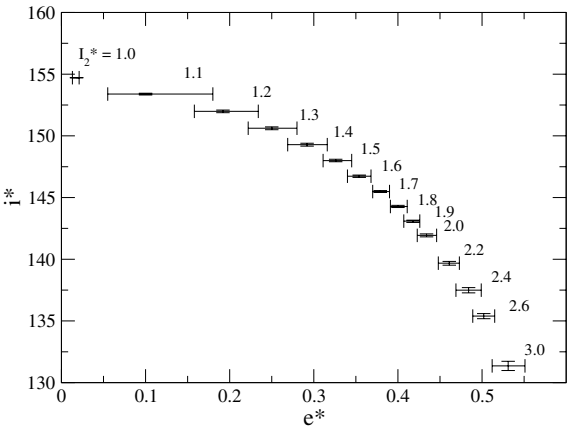

Figure 8. For $L^* = 1.04 \times 10^{-4}$ (i.e. $a^* = 0.13$ au) in the Saturn system, the plot shows values of i^* and e^* corresponding to the centre of the main libration island for different values of I_2^*. Error bars indicate the libration width in each orbital element.

construction of the dynamical maps is very time consuming, instead of repeating the calculations for other semimajor axes we have chosen to study the effects of a slow (adiabatic) migration on the satellite orbit. The planets were not affected by this migration and remained in fixed heliocentric orbits.

To simulate a smooth orbital decay we used the same procedure as described in Beaugé et al. (2006a), which consists in including a Stokes drag-like exterior force in the equations of motion. This additional non-conservative perturbation can be modified to introduce any desired change in both the semimajor axis and eccentricity. For all the integrations we adopted values such that the migration introduced no change in either the eccentricity or the inclination, but only a slow change in a^* with a characteristic time-scale equal to $\tau_a = 10^7$ years. This value is much larger than the librational period of θ^*, thus guaranteeing the adiabatic approximation.

Fig. 9 shows a typical example of an inward migration, where the initial condition corresponds to $a^* = 0.13$ au and $I_2^* = 1.5$ and a moderate amplitude of libration around $\theta^* = 0$. The integration was continued until the final semimajor axis was equal to $a^* \sim 0.06$ au (closer to the planet than the real irregular moons), and the output was filtered in the same manner as before. The top graph shows the variation of the resonant angle as a function of the semimajor axis, and the orbital evolution caused by the migration occurs from right to left. Although the particle remains trapped in the secular resonance throughout the integration, for smaller a^* it switches from an oscillation around $\theta^* = 0$ to an asymmetric libration and, finally, to a motion around $\theta^* = 180$. The change in amplitude after each bifurcation is due to the discontinuity in the action at these points. The bottom plot shows the change in i^* and e^* during the migration. The thick black curve was obtained applying an additional filter to the numerical data to eliminate the variations with periods similar to that of the resonant angle.

The same procedure was repeated for initial conditions for other values of I_2^* and extended to an outward migration of the satellite orbits. The resulting families in the (i^*, e^*) plane are plotted in Fig. 10. Each thick continuous curve shows the filtered evolution of the resonant orbit during the orbital migration and can be considered as the approximate location of the families of zero-amplitude solutions for different values of a^*. Empty rectangles show the location of the solutions for $a^* = 0.06$ au while diamonds correspond to $a^* = 0.19$ au. For larger semimajor axes, the orbital behaviour

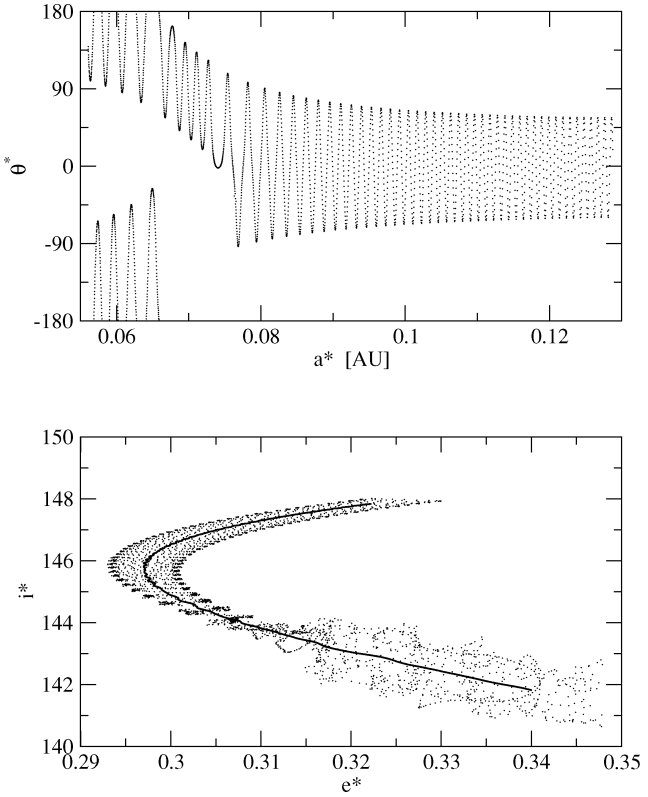

Figure 9. Simulation of the satellite orbital decay. The initial condition corresponds to a moderate amplitude $\theta^* = 0$ libration with $I_2^* = 1.5$ at $a^* = 0.13$ au. Migration only affects the satellite semimajor axis with $\tau_a = 10^7$ years. In the lower plot, the thick black curve is the filtered output over the resonant angle.

showed strong chaotic motion leading to an escape of the particles in short time-scales. The initial conditions (i.e. centre of libration for $a^* = 0.13$ au) are shown as empty circles. The dashed curves correspond to interpolated values calculated from the numerical solutions for all three semimajor axes.

The area inside the 'wedge'-shaped region gives a fair idea of the region covered by the $\nu_\odot$ resonance for retrograde orbits in the Saturn system, at least for the interval of a^* analysed. For high inclinations the libration domain occurs for low to moderate eccentricities, and the exact location depends strongly on a^*. However, as $i^* \to 90^\circ$, the resonance region shrinks until for $i^* < 130^\circ$ it is practically restricted to a single curve for all values of the semimajor axis.

6 SCALING LAW FOR OTHER SATELLITE SYSTEMS

The structure of the $\nu_\odot$ resonance shows the same dynamical structure when computed for fictitious retrograde satellites in the Jovian and the Saturn system. Although constructed for different values of planets and values of L^*, Figs 3 (Jupiter) and 6 (Saturn) appear basically the same, even if the values of I_2^* and the e^* of the librational centres are not equal. As a consequence, we wish to analyse whether there exists a simple transformation (or scaling) that allows us to deduce the main characteristics of the secular resonance around any planet, starting from the information obtained for Saturn.

Switching planets introduces two main effects: (i) a change in the semimajor axis $a_\odot$ of the planetocentric orbits of the Sun (to a

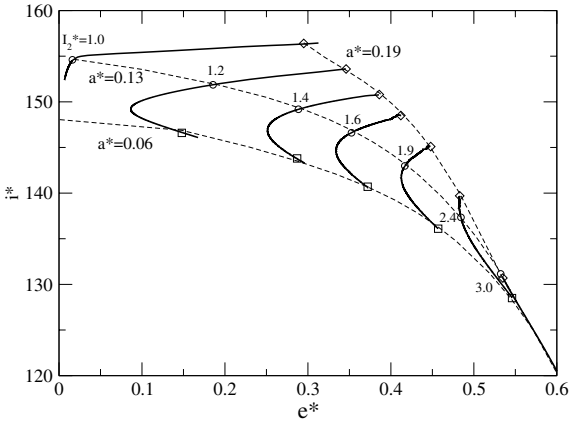

Figure 10. Thick continuous curves show the families of the centre of libration as obtained from inward and outward migration starting from $a^* = 0.13$ au. The initial value of I_2^* of each family is marked close to the initial position (empty circle). The inward migration was stopped at $a^* \simeq 0.06$ au and the corresponding solution marked with an empty square. The outward migration was continued until $a^* \simeq 0.19$ au. Here the final solution is marked with a diamond. Dashed curves show the interpolated families for the three values of a^* discussed above.

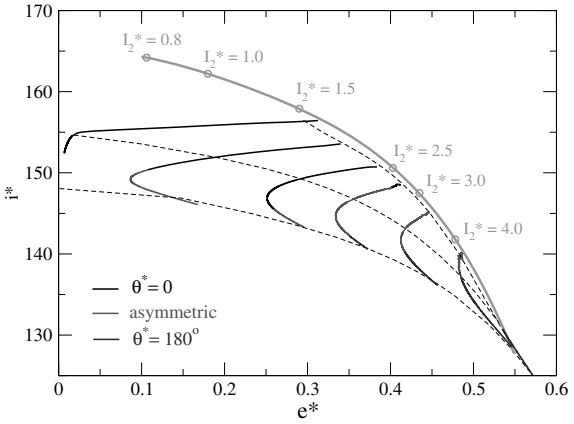

Figure 11. Families of the zero-amplitude resonant solutions, as a function of a^*, for retrograde orbits in the Saturn satellite system and six values of I_2^*. Black curves correspond to libration around $\theta^* = 0$, red to oscillations around asymmetric libration centres and blue to libration around $\theta^* = 180^\circ$. Dashed lines show interpolated curves for $a^* = 0.06$, $a^* = 0.13$ and $a^* = 0.19$ au. The thick green curve shows the interpolated family of solutions obtained for fictitious Jupiter satellites with $a^* = 0.16$ au (see Figs 3 and 4).

new value $a'_\odot$) and (ii) a change in the mass m_p of the planet (to a new value m'_p). The outer planets also differ in eccentricity and inclination, although these parameters can temporarily be considered fixed.

Allowing for a change in $a_\odot$ is fairly straightforward. Since the secular Hamiltonian (averaged over short-period terms) only depends on the ratio $a/a_\odot$ (e.g. Murray & Dermott 1999), the semimajor axis of the planet only appears as a normalizing factor in the dynamical system. Thus, it should be expected that the dynamical structure calculated at a^* in the first planet should correspond to the one located at $a'^* = \Gamma_a\, a^*$ in the second primary, where

$$\Gamma_a = \frac{a'_\odot}{a_\odot}. \tag{7}$$

A more complex task is trying to model the changes caused by differences in the planetary mass m_p. However, we can use an approximation of the restricted circular three-body problem (RC3BP) known as Hill's problem (Hill 1878, 1886; see also Szebehely 1967, section 10.4). Hill's equations, originally constructed as the basis of a lunar theory, are a simplified version of the RC3BP in which the more massive primary (i.e. Sun) is considered to be infinitely far away but its gravitational effects are still felt in the system. In a rotating coordinate system with position vectors $\boldsymbol{r}$ centred in the smaller primary (i.e. planet), it is possible to introduce a scaling $\boldsymbol{r} \rightarrow \bar{\mu}^{1/3}\boldsymbol{r}$ which yields equations of motion that are independent of the masses (at least to smallest order in $\bar{\mu}$). We denote $\bar{\mu}$ as the mass ratio between primaries. Consequently, the complete dynamical behaviour of the system can be deduced for any given value of $\bar{\mu}$ and extended to other masses just modifying the scaling parameter.

Hill's approximation assumes very small mass ratios, motion close to the smaller primary and circular orbits between both massive bodies. Although these conditions are not rigorously satisfied in our case, its results may still be used as a first approximation. We may then introduce a second scaling factor Γ_m defined as

$$\Gamma_m = \left(\frac{m'_\mathrm{p}}{m_\mathrm{p}}\right)^{1/3}, \tag{8}$$

which constitutes a new transformation in the coordinates due to changes in the planetary mass. Thus, given the complete change from one primary m_p to another of mass m'_p with different heliocentric semimajor axes, the original dynamical structure obtained at a^* should be reproduced at a new value given by

$$a'^* = (\Gamma_a \Gamma_m)\, a^*. \tag{9}$$

As a first test, Fig. 11 once again presents the families of zero-amplitude resonant solutions in the Saturn system (continuous black, red and blue curves) for smooth variations of L^*. However, now colours indicate the type of libration: black is used for motion around $\theta^* = 0$, red for asymmetric librations and blue for oscillations around $\theta^* = 180^\circ$. As already shown in Fig. 9, migration can cause changes in the mode of libration. The dashed curves show the interpolated location of the centres for $a^* = 0.06$, $a^* = 0.13$ and $a^* = 0.19$ au. Thus, for any other value of the proper semimajor axis it is possible, at least qualitatively, to estimate the locus of zero-amplitude solutions in the (e^*, i^*) plane and the corresponding type of libration.

As an example, let us consider the resonant maps constructed in the Jovian system for $a^* = 0.16$ (Fig. 3). The locus of resonant centres shown in Fig. 4 can be interpolated and is shown in Fig. 11 as a thick continuous green curve. The individual values are marked by open circles with the corresponding values of I_2^* placed adjacently. Applying the scaling law (9) we find that in the Saturn system this curve should correspond to $a'^* = 0.197$ au, placing it barely above the upper dashed line. Not only does the location of the green curve shows a very good correlation with the prediction of this simple scaling law, but there is also an agreement between the predicted type of resonant mode and the dynamical maps shown in Fig. 3. It is important to mention that the eccentricity adopted for each planetary body was equal to its individual present values.

In conclusion, the libration centres (both location and type) of fictitious satellites around Jupiter can be deduced from their counterparts in the Saturn system, simply applying the scaling law (9) to the original proper semimajor axis a^* and analysing the curve corresponding to the new a'^* in Fig. 11. However, we still need to analyse the structure of the resonance lobes in more detail and

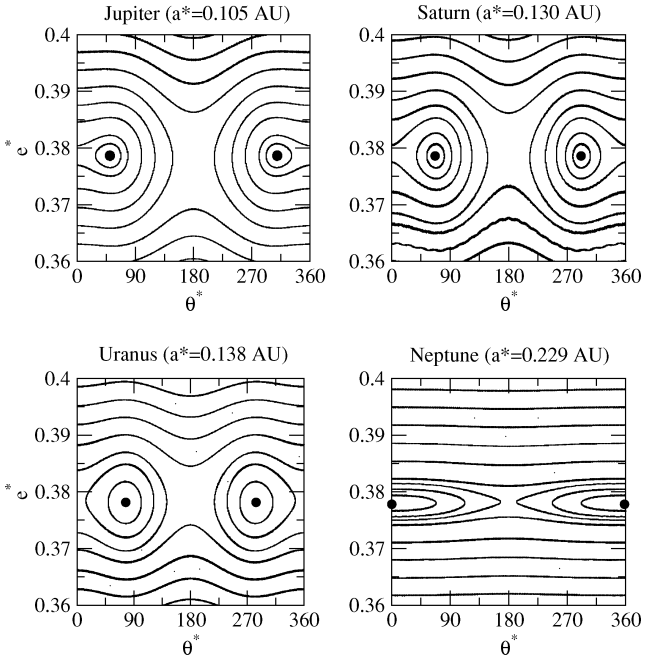

Figure 12. Resonant maps, around all giant planets, for initial conditions leading to the same location of the libration centre (black circle) in the (e^*, i^*) plane. Values of the proper semimajor axes are given on the top of each frame. While the first three maps are very similar, the low eccentricity of Neptune prevents the appearance of the asymmetric domain.

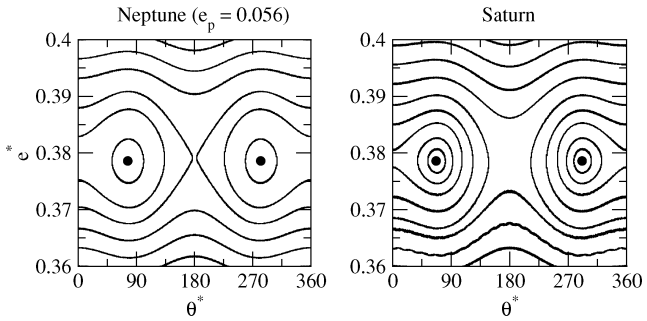

Figure 13. Same as Fig. 12, comparing the resonant maps for Neptune (left) and Saturn (right). However, the eccentricity of both planets is now considered the same and is equal to the osculating value of Saturn. The resonant structure in both frames is identical.

extend the study to other planetary masses. Results are shown in Fig. 12, where we present four dynamical maps, each for fictitious satellites around a different giant planet. Starting from Saturn, the values of L^* and I_2^* adopted for the other frames were deduced from the scaling law. The value of I_2^* was chosen close to the onset of the asymmetric librations, and thus constitutes a region particularly sensitive to changes in the dynamical system.

If the planetary eccentricities were taken the same, the resonant structure around all four outer planets would be identical. However, since the value of $e_\odot$ is different for each primary, the resonant structure must reflect this change. The location of the libration centre in e^* and i^* appears practically invariant, with $e^* \simeq 0.379$ in all four plots. Moreover, Jupiter, Saturn and Uranus have very similar orbital eccentricities, and therefore the type of libration (i.e. asymmetric) is maintained and the resonant domain has similar sizes. However, since $e_{\rm Sat} > e_{\rm Ura} > e_{\rm Jup}$, the libration lobe surrounding the asymmetric solution is larger in Saturn than in Uranus, while Jupiter presents the smallest region of the three.

Although the differences in topology of the resonant domain around the first three planets are not very significant, the map constructed for Neptune shows no asymmetric lobe and the libration occurs around $\theta^* = 0$. This, however, may be understood in terms of the planetary eccentricity $e_{\rm Nep} = 0.008$, much smaller than the other giant planets. Let us recall the first-order analytical model F_1^* presented by Yokoyama et al. (2003) and summarized in equation (3). Writing the coefficients A_i explicitly in terms of the perturber's eccentricity $e_\odot$, and retaining only smallest orders, we can express this function as

$$F_1^* = C_0 + C_1 e_\odot \cos(\theta^*) + C_2 e_\odot^2 \cos(2\theta^*), \quad (10)$$

where the new coefficients $C_i = C_i(I_1^*; L^*, I_2^*, m_{\rm p})$ are now independent of $e_\odot$. Although we have mentioned that this model is not a reliable representation of the dynamics of the $\nu_\odot$ resonance, the imprecision is only due to the values of the coefficients C_i. The functional form of the resonant Hamiltonian stems from the D'Alembert rules of any expansion of the perturbing potential, which specifies that, for any integer k, the terms associated with a k-order harmonic of θ^* must be proportional to $e_\odot^k$. Thus, any other Hamiltonian function, whatever its origin, will have the same form as (10).

Libration centres are specified by the conditions $\partial F_1^*/\partial I_1^* = \partial F_1^*/\partial \theta^* = 0$. In particular, the second condition explicitly reads as

$$\sin(\theta^*)\left(C_1 + 4C_2 e_\odot \cos(\theta^*)\right) = 0. \quad (11)$$

This equation has two trivial solutions ($\theta^* = 0$ and $\theta^* = 180^\circ$) which correspond to symmetric librations. However, if

$$4\,|C_2|\,e_\odot > |C_1|, \quad (12)$$

the contribution of the second harmonic in the resonant angle is larger than the first, and asymmetric librations are possible (see Beaugé 1994 for a similar analysis for exterior mean-motion resonances in the asteroidal problem). Since C_1 and C_2 vary differently as a function of L^* and I_2^*, we can explain why asymmetric librations are found for some values of the inclination and not for others. However, condition (12) depends linearly on the planetary eccentricity. Thus, if $e_\odot$ is sufficiently small, asymmetric solutions are not possible and all librations are of the symmetric type. This appears to be the case of the Neptune satellite system, at least for the values of L^*, I_2^* analysed.

As a final test, Fig. 13 shows a comparison of the resonant structure of two systems: the plot on the right reproduces the dynamics around the asymmetric libration lobe in Saturn (top-right frame of Fig. 12), while the left-hand plot was obtained for a fictitious Neptune in which the planet's eccentricity was elevated to the same value as Saturn. As expected, the resonant structure is now equivalent, confirming that the absence of asymmetric librations in Fig. 12 is in fact due to the planet's quasi-circular orbit.

7 CONCLUSIONS

We have presented a numerical study of the structure of the $\nu_\odot$ secular resonance for retrograde satellites around the giant planets. This commensurability is associated with a libration of the secular angle $\theta = \varpi - \varpi_\odot$, where $\varpi = \Omega - \omega$ is the longitude of the pericentre of the irregular moon and $\varpi_\odot$ the corresponding angle for the planetocentric orbit of the Sun. We have shown that the resonant domain presents a diversity of libration modes, including both

symmetric and asymmetric librations. Each mode appears restricted to certain intervals of the mean–mean inclination i^* of the satellite. Librations around $\theta = 0$ occur for large values of i^* (typically $i^* \gtrsim 150^\circ$), while oscillations around $\theta = 180^\circ$ seem to dominate for $i^* \lesssim 140^\circ$. Asymmetric solutions appear at intermediate inclinations, although planets with very small eccentricities (such as Neptune) may not contain asymmetric solutions at all. Calculating the mean–mean inclination for real irregular satellites shows a good agreement with these predictions. Both Pasiphae ($i^* = 148^\circ$) and Sinope ($i^* = 157^\circ$) display librations around $\theta = 0$, while the resonant angle of Narvi ($i^* = 141^\circ$) is in an asymmetric mode.

Simulating a smooth orbital migration of satellite orbits has shown that the resonant lock is maintained as long as the adiabatic condition is met; in other words, the characteristic time-scale of the orbital variation is much longer than the libration period. We have used these results to map the location and type of libration centres as a function of the proper semimajor axis, thus giving a more global view of the region of the phase space dominated by the $\nu_\odot$ commensurability.

Finally, we presented a simple scaling law that can be used to relate the resonant structure in any the satellite system. Since Jupiter, Saturn and Uranus have similar orbital eccentricities, it is expected that the structure of the secular resonance should also be very similar, except for a scaling in the semimajor axis of the irregular moons. Neptune, however, has an almost circular orbit, which inhibits the formation of asymmetric libration points. For satellites around this planet, it is expected that symmetric solutions should dominate.

From the scaling law, it can be shown that a change in the semimajor axis of the satellite is equivalent to a similar one on the planet. In other words, the same results would be obtained if the heliocentric semimajor axis of the planet suffered a slow migration while the planetocentric orbit of the moon was kept fixed. Although we have only done a few simulations with a fast (non-adiabatic) migration, it appears that the resonant configuration is not so easily preserved, and any originally librating body was usually expelled from the resonance. However, additional simulations are required to confirm that this behaviour is general.

In this paper we have considered only the restricted three-body problem and, consequently, neglected the gravitational effects of the other giant planets. This is indeed an approximation, since these additional perturbations may cause significant orbital variations (e.g. Carruba et al. 2004; Ćuk & Burns 2004). In particular, the temporary nature of the $\nu_\odot$ resonance lock of real satellites is due to the gravitational effects of the other planetary bodies. In consequence, the results presented here must be viewed only as a starting ground for the complete secular behaviour for retrograde irregular moons. The full picture will surely be far more complex.

ACKNOWLEDGMENTS

This work has been supported by the Cordoba National University (Secyt-UNC) and the Argentinian Research Council (CONICET).

REFERENCES

Beaugé C., 1994, Celestial Mechanics Dynamical Astron., 60, 225
Beaugé C., Nesvorný D., 2007, AJ, 133, 2537
Beaugé C., Michtchenko T. A., Ferraz-Mello S., 2006a, MNRAS, 365, 1160
Beaugé C., Nesvorný D., Dones L., 2006b, AJ, 131, 2299
Carpino M., Milani A., Nobili A. M., 1987, A&A, 181, 182
Carruba V., Nesvorný D., Burns J. A., Ćuk M., Tsiganis K., 2004, AJ, 128, 1899
Cincotta P. M., Simó C., 2000, A&A, 147, 205
Ćuk M., Burns J. A., 2004, AJ, 128, 2518
Hill G. W., 1878, American J. Math., 1, 5
Hill G. W., 1886, American J. Math., 8, 1
Hinse T. C., Christou A. A., Alvarellos J. L. A., 2009, MNRAS, submitted (arXiv:0907.4886)
Kaula W. M., 1962, AJ, 67, 300
Kozai Y., 1962, AJ, 67, 591
Lidov R., 1961, Analiz Evolucii Orbit Iskustvennich Sputnikov, Problemi Dvigenia Iskustvennich Nebesnich Tel. Izd. Akad. Nauk SSSR, Moscow, p. 119
Murray C. D., Dermott S. F., 1999, Solar System Dynamics. Cambridge Univ. Press, Cambridge, chapter 6
Nesvorný D., Alvarellos J. L. A., Dones L., Levison H. F., 2003, AJ, 126, 398
Nicholson P. D., Cuk M., Sheppard S. S., Nesvorny D., Johnson T. V., 2008, in Barucci M. A., Boehnhardt H., Cruikshank D. P., Morbidelli A., eds, The Solar System Beyond Neptune. Univ. Arizona Press, Tucson, p. 411
Saha P., Tremaine S., 1993, Icarus, 106, 549
Szebehely V., 1967, Theory of Orbits. Academic Press, New York
Whipple A., Shelus P. J., 1993, Icarus, 101, 265
Wintner A., 1941, The Analytical Foundations of Celestial Mechanics. Princeton Univ. Press, Princeton, NJ
Yokoyama T., Santos M. T., Cardin G., Winter O. C., 2003, A&A, 401, 763

This paper has been typeset from a TEX/LATEX file prepared by the author.